Supporting information for: Facile measurement of the rotation of a single optically trapped nanoparticle using the diagonal ratio of a quadrant photo-diode

Yuval Yifat,[†,‡] John Parker,[†,¶] Tian-Song Deng,[†,⊥] Stephen K. Gray,[§] Stuart A. Rice,[†,∥] and Norbert F. Scherer[*,†,∥]

†*James Franck Institute, The University of Chicago, 929 E. 57th Street, Chicago, Illinois 60637, USA*

‡*Innoviz Technologies Ltd, 2 Amal Street, Rosh Ha-Ayin, 4809202, Israel*

¶*Department of Physics, The University of Chicago, 929 East 57th Street, Chicago, Illinois 60637, USA*

§*Center for Nanoscale Materials, Argonne National Laboratory, 9700 South Cass Avenue, Argonne, Illinois 60439, USA*

∥*Department of Chemistry, The University of Chicago, 929 East 57th Street, Chicago, Illinois 60637, USA*

⊥*School of Electronic Information, Hangzhou Dianzi University, No. 1158, 2nd Avenue, Baiyang Street, Hangzhou, 310018, China*

E-mail: nfschere@uchicago.edu

S1. TEM Measured particle shapes and Aspect Ratios

The variance in the measured rotational frequencies for both the 150nm and the 200 nm Ag nanoparticles implies a dispersion in the size and aspect ratio (AR) of the particles. Such a dispersion in spinning rates has been reported for similar experiments in the literature[S1]. We confirmed the existence of a distribution of nanoparticle shapes (and sizes) by imaging them using electron microscopy.

The particles were drop cast on a copper grid and imaged using a transmission electron microscope (TEM; FEI Tecnai F30 300kV FEG) at a magnification of x145k (see Figure $S1$(a,b)). We calculated the AR of the TEM images by fitting them to an ellipse and calculating the ratio between their major (long) axis and their minor axis. Figure $S1$(c) shows the distribution of AR's for 150 nm (blue connected dots) and 200 nm (red connected dots) NPs. As can be seen from the histograms, the particles are not uniformly spherical and the distribution has a mean AR that is greater than 1. The 150 nm Ag nanoparticles were measured to have an $AR = 1.09 \pm 0.06$ (n=16); The 200 nm Ag nanoparticles were measured to have an $AR = 1.22 \pm 0.16$ (n=10).

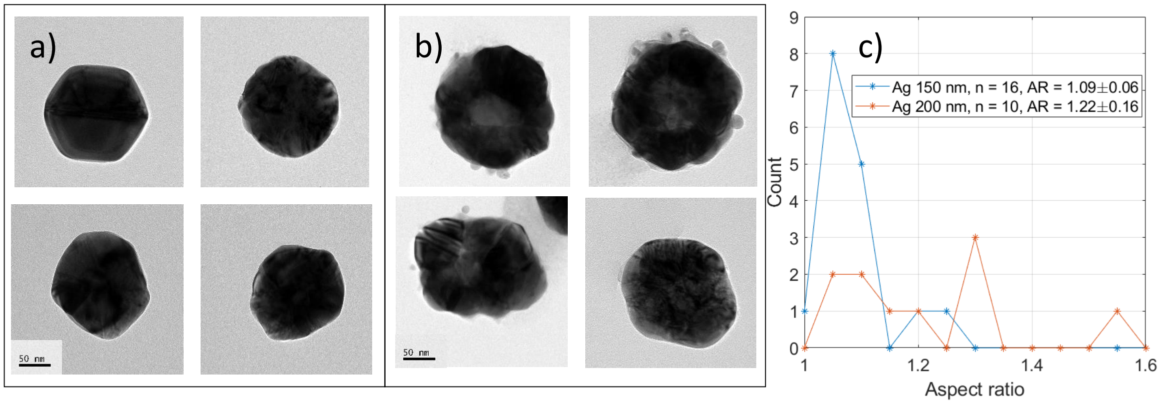

Figure S1: Representative TEM images of **(a)** 150 nm Ag nanoparticles and **(b)** 200 nm Ag nanoparticles. Images were captured at a magnification of x145k. Scale bars are 50 nm. **(c)** Histogram of AR calculated from images of nanoparticles. Mean AR values mentioned in legend.

The larger mean AR and variance for the 200 nm nanoparticles, as compared to those calculated for the 150 nm nanoparticle suggest that the dispersion in spinning rates of the 200 nm Ag nanoparticles would be greater than for the 150 nm nanoparticles. While we see a significant dispersion in both nanoparticle sizes (e.g. Fig 3(c,d) in the main text), it is not immediately evident that the dispersion is larger for the 200 nm particles. A full understanding of the spinning dynamics needs to take into account the full hydrodynamic effects of a particle spinning in the water, and this is addressed in section S2 (T-matrix-Langevin Dynamics).

Note that the AR values captured in the TEM measurements are calculated on 2D projections of the nanoparticles as opposed to their 3D shapes[S2], adding uncertainty to the exact AR of individual measured NPs. Furthermore, we cannot know whether the particles are oblate or prolate. Nonetheless, in previous work we have measured Ag nanoparticle extinction spectra (which are dominated by their scattering corss-section) using a UV-Vis spectrophotometer, and confirmed that the light scattered from them matches the expected Mie scattering resonances from spherical particles[S3]. Thus we expect that the actual AR values we measure should be close to the mean value of the (spherical) particle size.

S2.T-matrix-Langevin Dynamics

We utilized the T-matrix method[S4] to simulate the electrodynamic interaction of the laser beam with a single anisotropic nanoparticle. For simplicity, we consider a spheroidal nanoparticle with minor radii a and major radius b, so that its dimensions are (a, a, b). Instead of using a and b to classify the nanoparticle, we use the spheroid's aspect ratio $\delta = b/a$ and the its equivalent radius $r_{\mathrm{eq}} = (a^2 b)^{1/3}$. When $\delta > 1$, the spheroid is prolate and when $\delta < 1$ it is oblate. The equivalent radius is the radius of a sphere that can be deformed into the spheroid, preserving its volume.

The T-matrix of the spheroid is calculated using the Null-Field Method with Discrete-Sources (NFM-DS).[S5] The T-matrix relates the spherically incident wave coefficients to the spherically outgoing wave coefficients

$$p^{\text{scat}} = \mathcal{T} p^{\text{inc}} \tag{S1}$$

The incident field coefficients p^{inc} are calculated using a quadrature method on the angular spectrum of the incident laser beam.[S6] The T-matrix then provides the scattering coefficients p^{scat} of the spheroid. With both incident and scattering coefficients determined, there exist analytic expression for the time-average electrodynamic force and torque acting on the spheroid obtained from integrating the Maxwell Stress Tensor.[S7]

The electrodynamic force F and torque τ acting on the spheroid are inserted into an overdamped Langevin equation of motion for the nanoparticle velocity v and angular velocity ω

$$v_i(t) = M_{ij}(t)\left[\alpha_{kl}(t)\eta_k(t) + F_j(t)\right] \tag{S2}$$

$$\omega_i(t) = M_{ij}(t)\left[\alpha_{kl}(t)\eta_k(t) + \tau_j(t)\right] \tag{S3}$$

Here, M_{ij} is the spheroid's mobility matrix, η is a normal random vector with mean 0 and variance 1, and α_{kl} is a matrix chosen such that the fluctuation-dissipation theorem is valid, i.e., $2k_BTM_{ij}^{-1} = \alpha_{ik}\alpha_{kj}$, where T is the temperature of the bath. α_{kl} is constructed by performing a Cholesky decomposition of $2k_BTM_{ij}^{-1}$ at every time-step in the Langevin equation. The mobility matrix M_{ij} has an analytic expression for spheroids that is provided elsewhere.[S8]

To obtain the trajectory of the spheroid, the linear velocity and angular velocity are used to update the position and orientation of the particle at every time step. The position is updated by an amount $d\boldsymbol{r} = \boldsymbol{v}(t)\Delta t$, where Δt is the time-step. The orientation is represented by a quaternion $\boldsymbol{q}$, and is updated by an amount $d\boldsymbol{q} = \boldsymbol{q}_\omega(t) \cdot \boldsymbol{q}(t)\Delta t/2$, where $\boldsymbol{q}_\omega(t) = (\omega, 0)$ is a quaternion constructed from the angular velocity.[S9]

Finally, before the next time-step is run and the electrodynamics is solved for, the T-matrix of the spheroid must be updated since the particle has rotated. Fortunately, the T-matrix need not be recomputed since the T-matrix has an analytically known way of being rotated.[S10] Given the T-matrix of an object in a fixed reference frame, $\mathcal{T}_0$, the T-matrix at any time can be constructed as

$$\mathcal{T}(t) = D(t)\mathcal{T}_0 \left[D(t)\right]^{-1} \tag{S4}$$

where $D(t)$ is the Wigner-D matrix corresponding to the quaternion $\boldsymbol{q}(t)$. The electrodynamic force and torque can now be calculated at the next time-step, and the trajectory of the spheroid can be obtained through successive time-steps.

S3. Theoretical calculation of rotational dynamics dependence on nanoparticle aspect ratio

Two important overdamped rotational dynamical quantities are the spheroid's average angular velocity around the z-axis, $\overline{\omega_z(t)}$, and the rotational diffusion coefficient, $D_r(t)$, given by

$$\begin{aligned}
\overline{\omega_z(t)} &= \tau_z/\gamma \\
D_r(t) &= \frac{1}{2t}\overline{\left(\phi_z(t) - \overline{\omega_z(t)}t\right)^2} = \frac{k_B T}{\gamma}
\end{aligned} \tag{S5}$$

where T is the temperature of the bath, τ_z is the electrodynamic torque from the trapping beam, γ is the spheroid's rotational drag coefficient, and ϕ_z is the angle the particle has rotated along the z-axis. For small particles, the torque acting on the spheroid due to a circularly polarized Gaussian beam is approximately[S11,S12]

$$\tau_z = \frac{2P}{\pi w_0^2}\left[\alpha V + \beta V^{2/3}(\delta-1)^2\right] = \frac{8P}{3w_0^2}\left[\alpha r_{\text{eq}}^3 + \beta r_{\text{eq}}^2(\delta-1)^2\right] \tag{S6}$$

where P is the laser power, w_0 is the beam width at the focus, and α and β are constants intrinsic to the spheroid's material. The first term in Equation (S6) is a torque due to the absorption of circularly polarized photons and is proportional to the volume; the second term is a torque due to asymmetric scattering of photons due to the anisotropy of the particle and is proportional to its cross-sectional area. For silver at $\lambda = 800\,\text{nm}$, $\alpha = 1.61 \times 10^{-10}\,\text{N/m}^2$ and $\beta = 4.01 \times 10^{-14}\,\text{N/m}$ (values of α, β fitted based on experimentally measured dielectric function [S13].

The rotational drag coefficient of the spheroid is approximately [S8].

$$\gamma \approx \frac{16}{5}\pi r_{\text{eq}}^3 \mu \left(\delta + \frac{3}{2}\delta^{-1}\right) \approx 8\pi r_{\text{eq}}^2 \mu \tag{S7}$$

where μ is the viscosity of the fluid. Equation (S6) and Equation (S7) can be plugged into Equation (S5)

$$\overline{\omega_z} = \frac{P}{3\pi w_0^2 \mu}\left[\alpha + \frac{\beta}{r_{\text{eq}}}(\delta-1)^2\right] \tag{S8}$$

$$D_r = \frac{k_B T}{8\pi r_{\text{eq}}^3 \mu} \tag{S9}$$

Note that the rotational diffusion in Equation (S9) is independent of the aspect ratio in this approximation. These equations can be inverted to obtain r_{eq} and δ (the equivalent radius and aspect ratio as defined in section S2)

$$r_{\text{eq}} = \left(\frac{5kT}{16\pi\mu D_r}\right)^{1/3} \tag{S10}$$

$$\delta = 1 + \sqrt{\frac{r_{\text{eq}}}{\beta}\left(\frac{3\pi w_0^2 \mu}{5P}\overline{\omega_z} - \alpha\right)} \tag{S11}$$

Thus, if the angular velocity and rotational diffusion of a particle can be measured in experiment, estimates can be made for the size and aspect ratio of the particle. The exact dependence of angular velocity and rotational diffusion on particle size and aspect ratio is calculated in Figure S2.

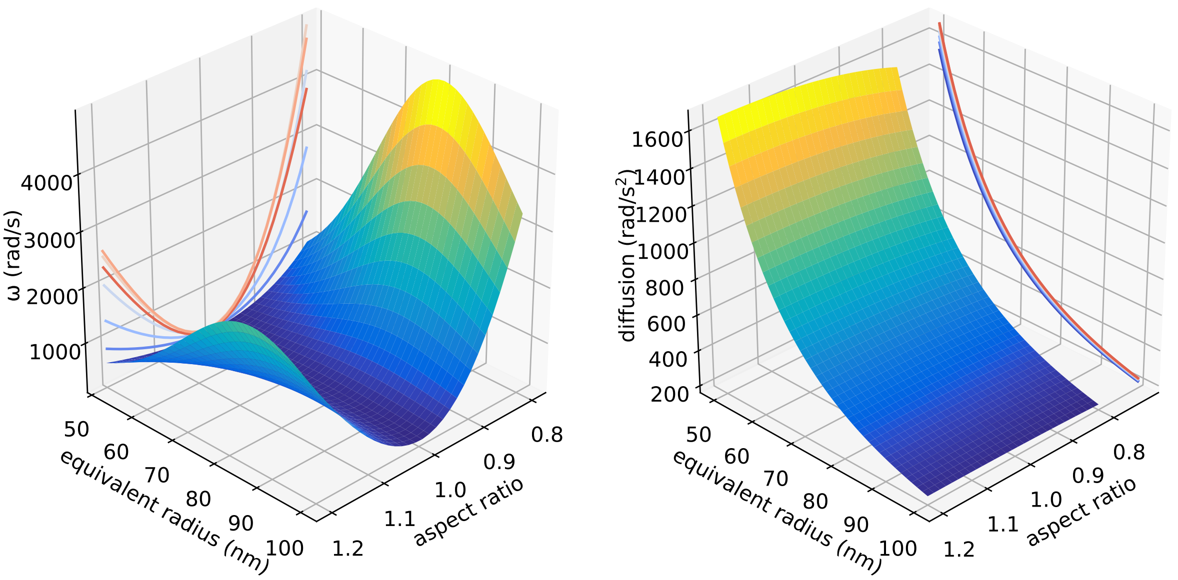

Figure S2: Rotational spinning and diffusion of a spheroidal silver nanoparticle. (left) Calculated angular velocity of an Ag nanoparticle in circularly polarized Gaussian beam ($w_0 = 1200\,\text{nm}$, $P = 28\,\text{mW}$) at variable equivalent radius and aspect ratio. (right) Calculated rotational diffusion coefficient for the same parameters.

S4. Minimal measured rotational frequency for transverse and diagonal QPD ratios

As mentioned in the main text, using the diagonal ratio of the QPD allows more sensitive measurement of the spinning and rotational dynamics of trapped NPs and at lower frequencies than is possible when using the transverse ratios obtained from traditional QPD measurements. A representative example of this is shown in Figure $S3$ which displays the PSDs of a single 200 nm Ag nanoparticle trapped in a Gaussian optical trapping beam of different optical powers.

When the incident optical power is high (e.g. the 9 mW intensity shown in Figure S3 panel (d), the spinning frequency, f_s, of the particle can easily be determined from the the transverse PSD (blue spectrum) where we observe a resonance peak at $f_{trans} = f_s = 2.5\,\mathrm{kHz}$. The diagonal ratio PSD (red spectrum) exhibits a peak at $f_{diag} = 2f_s = 5\,\mathrm{kHz}$. However, decreasing the incident optical power decreases the spinning frequency, and the resonance peak in the transverse ratio PSDs grows less distinct (e.g. Figure $S3$(c,b)) and finally disappears into the baseline, i.e., $1/f$ noise (Figure $S3$(a)). Conversely, the diagonal ratio PSD allows observing the rotational frequency of the particle even at the lowest measured incident power ($S3$(a), where $f_{diag} = 2f_s = 0.5\,\mathrm{kHz}$.)

Figure $S3$(e) shows a histogram of the number of particles for which we were able to resolve the rotational frequency as a function of trapping power for both the diagonal and the transverse QPD ratios. Note that we were able to ascertain the rotational frequencies of all NPs ($n = 13$) with the diagonal ratio measurement, but only about half using the transverse ratio at a low trapping power of 4 mW. For a majority of the particles, the rotational frequencies were observed using the diagonal ratio even at the minimal power of 2 mW. In contrast, using the transverse ratio, we were able to discern the rotational spinning information for all the particles only at 9 mW. These results demonstrate how the diagonal ratio allows more sensitive measurements of slower spinning particles than the transverse

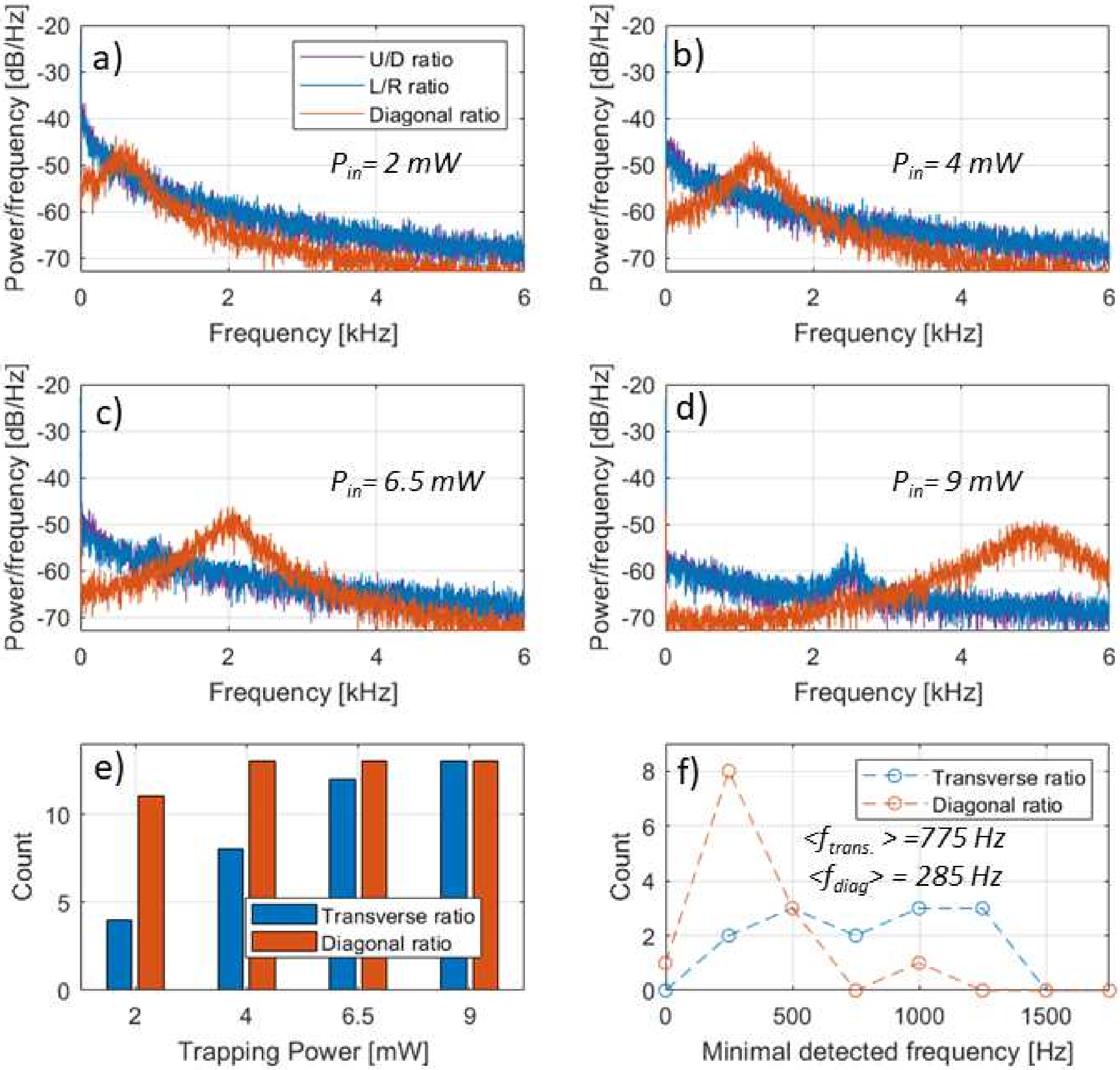

Figure S3: Minimal measured spinning frequencies from QPD diagonal and transverse ratios. **(a)** PSD plots of 200 nm Ag nanoparticles spinning in a circularly polarized (CP) Gaussian trap. Input power was 2 mW. Note the appearance of a resonance in the diagonal ratio signal at 500 Hz, corresponding to a spinning frequency of 250 Hz. There is no evidence of spinning in the transverse ratios. The same particle measured in the trap with input powers of **(b)** 4 mW. **(c)** 6.5 mW and **(d)** 9 mW. **(e)** The number of particles with a resolved spinning frequency as a function of trapping power. Note that by using the diagonal ratio the rotational frequency is resolved for all particles even at low optical powers. **(f)** Histogram of the lowest spinning frequency observed for 13 nanoparticles. Mean f_s values for lowest observed rotational frequencies of the transverse and diagonal ratios appear on the figure (note that for diagonal ratio, the spectral peak in the PSD is double the spinning frequency).

ratios.

This greater sensitivity of the diagonal measurement can also be seen by analyzing he lowest measured rotational frequency for the particles using both ratios. Figure $S3$(f) shows a histogram of the lowest detected spinning frequency of 13 200 nm Ag NPs trapped in the CP Gaussian trap. As the results measured at 2 mW exemplify it is clear that the diagonal ratio allows identification of significantly lower spinning frequencies, measured at lower trapping powers, than the transverse ratio. Therefore, the diagonal ratio allows tracking and, in principle, controlling NPs at lower optical trapping powers and rotational frequencies.

S5. FDTD Simulation of asymmetric scattering

The asymmetric scattering recorded by the QPD for a rotating particle can be understood by analyzing the scattered fields from the particle using finite difference time domain (FDTD) simulation. Using Lumerical FDTD software[S14] we simulated a spherical Ag nanoparticle with a diameter of 150 nm (refractive index of $n = 0.04 + 5.5i$) immersed in water ($n = 1.33$) near a glass interface ($n = 1.45$). The simulation grid size was set to 2 nm.

We illuminated the particle with a focused Gaussian beam of 790 nm wavelength, with a FWHM diameter of 500 nm and RHC polarization (similar to that of the experimental setup). The propagation direction of the simulated laser beam was in the $+z$ direction. We placed a far-field monitor in the z direction to capture the back reflection towards the QPD (in accordance with the trapping setup shown in Figure 1 in the main text). From the calculation of the far-field projection of the scattered field we were able to simulate the total optical intensity impinging in each quadrant of the QPD.

We proceeded to simulate the scattering from an almost spherical object by adding a small perturbation to the Ag nanoparticle. The perturbation we chose was a 20 nm Ag nanosphere that was placed at the equator of the 150 nm nanoparticle at different orientations (for fixed particles) serving as an asymmetric 'bump' on the NP. An analagous FDTD simulation was performed to capture the back-scattered intensity in the far-field, which is projected onto the QPD. Figure $S4$ shows the results of the simulations for both the perturbed (i.e. with asperity) and the unperturbed Ag nanosphere. Figure $S4$(a,i-v) show the $x - y$ maps of the refractive index of the nanoparticle in the different simulated conditions. Figure $S4$(b, i-v) displays the total intensity maps of the back-scattered light. Note that they are almost identical because the scattering for the perturbation is small compared to the scattering from the Ag nanoparticle.

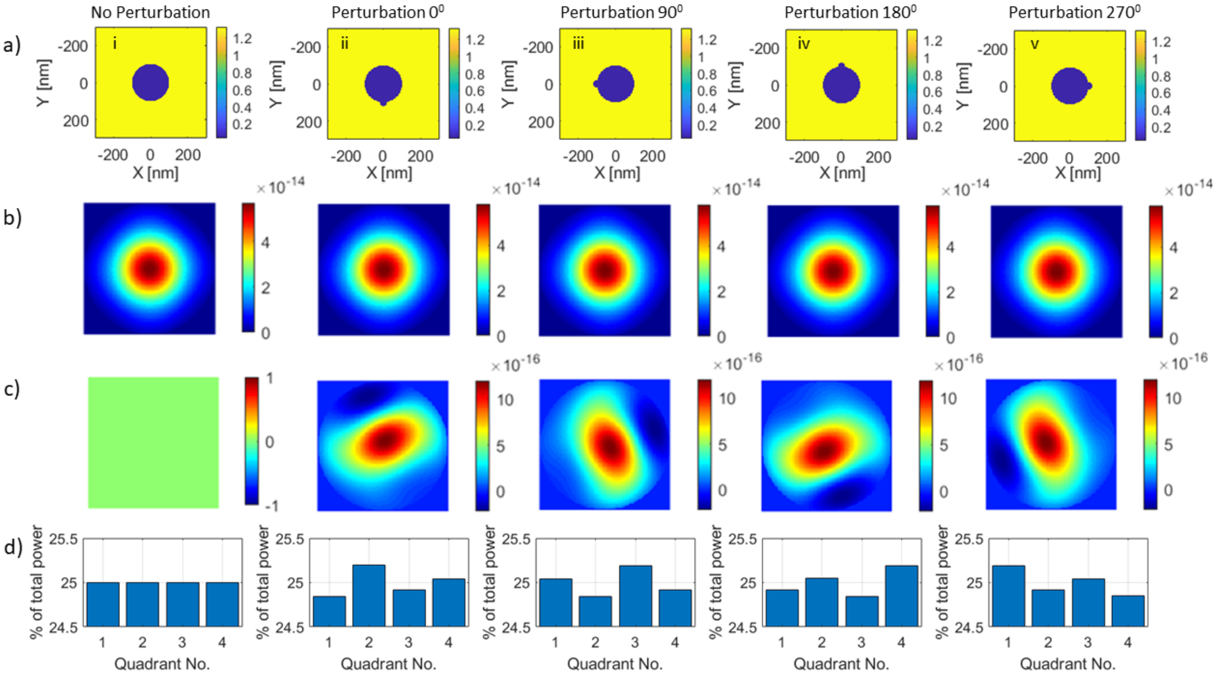

Figure S4: FDTD simulation results for back-scattering for spherical and slightly aspherical NPs. **(a)** Refractive index maps of a spherical NP (i) and NPs with a perturbation at different orientation (ii-v). **(b)** Total back-scattered intensity of each of the particle orientations. Differences between the simulated scattering from spherical and perturbed (aspherical) particles are not observable by eye due to the small size of the perturbation compared to the scattering from the simulated 150 nm NP. **(c)** Difference in the back-scattered intensity between each of the NP orientations and the unperturbed (spherical) NP. **(d)** Comparing the numerically integrated intensities of the NP scattering shown in **(b)**, divided into the four quadrants of the QPD. Note that the unperturbed particle shows a uniform signal on all 4 quadrants (i.e. **(d,i)**), while the perturbed NPs at different orientations show differences in the intensity collected by the four quadrants (i.e. **(d,ii-v)**).Furthermore, the ratios change with the orientation of the particle, in agreement with experiment.

The difference in scattering between the different configurations can be appreciated by calculating the difference between the scattered intensity of the perturbed ('bumpy') particles and the unperturbed particle. Figure $S4$(c, i-v) shows the differences between the particles for each configuration, I_{diff}. Note that I_{diff} is asymmetric and has local minima in the field (dark spot) oriented opposite to the perturbation position. This minimum is due to destructive interference between the field scattered from the large particle and the field scattered from the perturbation and rotates with the particle.

By dividing the total scattered intensity into four equal quadrants we can integrate the total power seen by each quadrant of the QPD for each particle orientation as shown in Fig. $S4$(d, 1-v). When an unperturbed particle is placed in the trap, the scattered intensities captured by each quadrant are nearly identical (see Fig $S4$(d,i)) small differences are due to numerical precision and the finite grid size. When the scattering from a particle with a perturbation is calculated, the asymmetries shown in Fig $S4$(c, ii-v) cause noticeable differences in the powers captured by each quadrant.

Rotation of the perturbed (aspherical) particle results in a shift in the power distribution between the quadrants. This can be seen in Fig. $S5$, where we rotated a perturbed particle between the 4 different perturbation orientations (Fig. $S5$(a); the angles chosen were $0^0, 90^0, 180^0$ and 270^0, same as $S4$) and calculated the resultant QPD ratios (Fig. $S5$(b)).

As can be seen in Fig. $S5$(b), the range of the diagonal ratio values is greater than that of the U/D and L/R ratios. Furthermore, the frequency of the diagonal ratio is twice that of the transverse ratios, in agreement with the experimental observations in the main text.

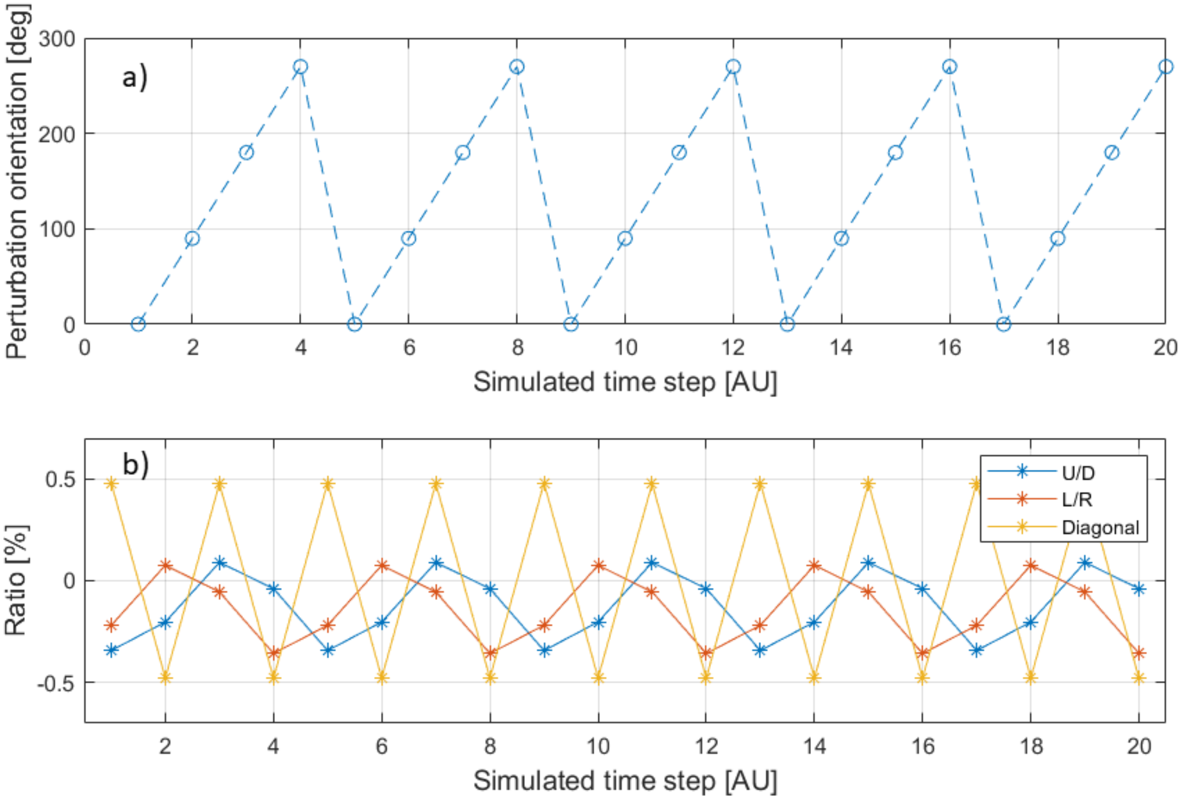

Figure S5: Time evolution of QPD resulting from simulated back-scattered far-field intensities. (a) Angular position of the perturbation as a function of time. (b) Transverse and diagonal ratios from the simulated QPD calculated from the simulated back-scattered fields. Ratios were calculated from the percentage of light collected on each QPD quadrant (see Figure $S4$(d,ii-v))

S6. Trapping of ultra-spherical Au nanoparticles

We further demonstrate the sensitivity of the QPD diagonal ratio measurement by repeating the trapping experiment on ultra-spherical Au nanoparticles (Nanocomposix; PVP coated, AUXU150). The experiment was performed under the same experimental conditions as with the Ag NPs described elsewhere in the text. Since the Au NPs are more spherical than the Ag NPs of the same diameter, we expect that the scattered field from them will be smaller, and the signal on the QPD will be smaller.

We measured the AR of the Au nanoparticles using the same TEM system described in Section S1 (TEM; FEI Tecnai F30 300kV FEG) and a magnification of x145k (see Figure $S6$(a,b)). Panel (a) shows representative TEM images of the Au nanoparticles (scale bar is 50 nm). Panel (b) shows the results of the measured AR for the Au nanoparticles compared to the data from the Ag nanoparticles discussed above. The Au nanoparticles (black connected dots) have $AR = 1.06 \pm 0.05$; n=32. This AR is lower than the Ag nanoparticles of diameter 150 nm Ag nanoparticles ($AR = 1.09 \pm 0.06$; n=16) and 200 nm ($AR = 1.22 \pm 0.16$; n=10)

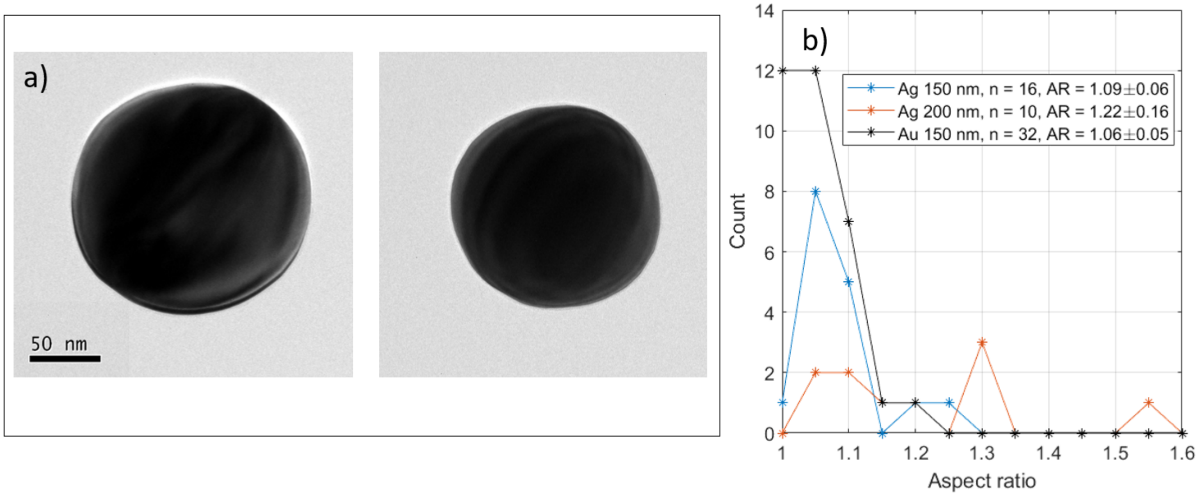

Figure S6: **(a)** Representative TEM images of ultra-spherical Au nanoparticles 150 nm Au nanoparticles. Images were captured at a magnification of x145k. Scale bars are 50 nm. **(c)** Histogram of AR calculated from images of nanoparticles (along with Ag NPs shown in section S1). Mean AR values and STD are mentioned in legend.

Figure $S7$ shows representative experimental data from a trapping experiment of an ultra-spherical Au NP (Figure $S7$(a,b)) compared to the trapping of a standard 150 nm Ag NP $S7$(c,d). Both particles were trapped in the same experimental conditions (4 mW trapping power, RH-CP). The time series in the Fig. $S7$(a,c) demonstrate that the voltage ratios collected from the Ag NPs are significantly larger than from the Au ultra-spherical NPs. As a result, the rotational peaks seen in the resultant PSDs are much stronger for 150 nm diameter Ag NPs than for 150 nm Au NPs (Fig. $S7$ (b,d)). The difference in the signal levels is due to the difference in scattering between the two NP types. The Ag NPs are not perfectly spherical and their imperfections act as the perturbations (such as those described in our simulations described in section S5) that increase the scattered field. By contrast, the Au NPs are smoother and the field scattered from them is smaller, leading to smaller voltage differences between the QPD segments in the time series (Fig $S7$(a) compared to Fig $S7$(c)) and a lower SNR peak in the PSD (Fig. $S7$(b) compared to Fig. $S7$(d)).

In fact, the rotational peak for the Au NP is only barely observable in the diagonal ratio, and is un-resolvable in the transverse ratio. This example demonstrates the sensitivity of the diagonal ratio of the QPDs in cases where the use of transverse ratios or other measurement methods (such as auto-correlation) would not be sensitive enough to detect the rotational motion.

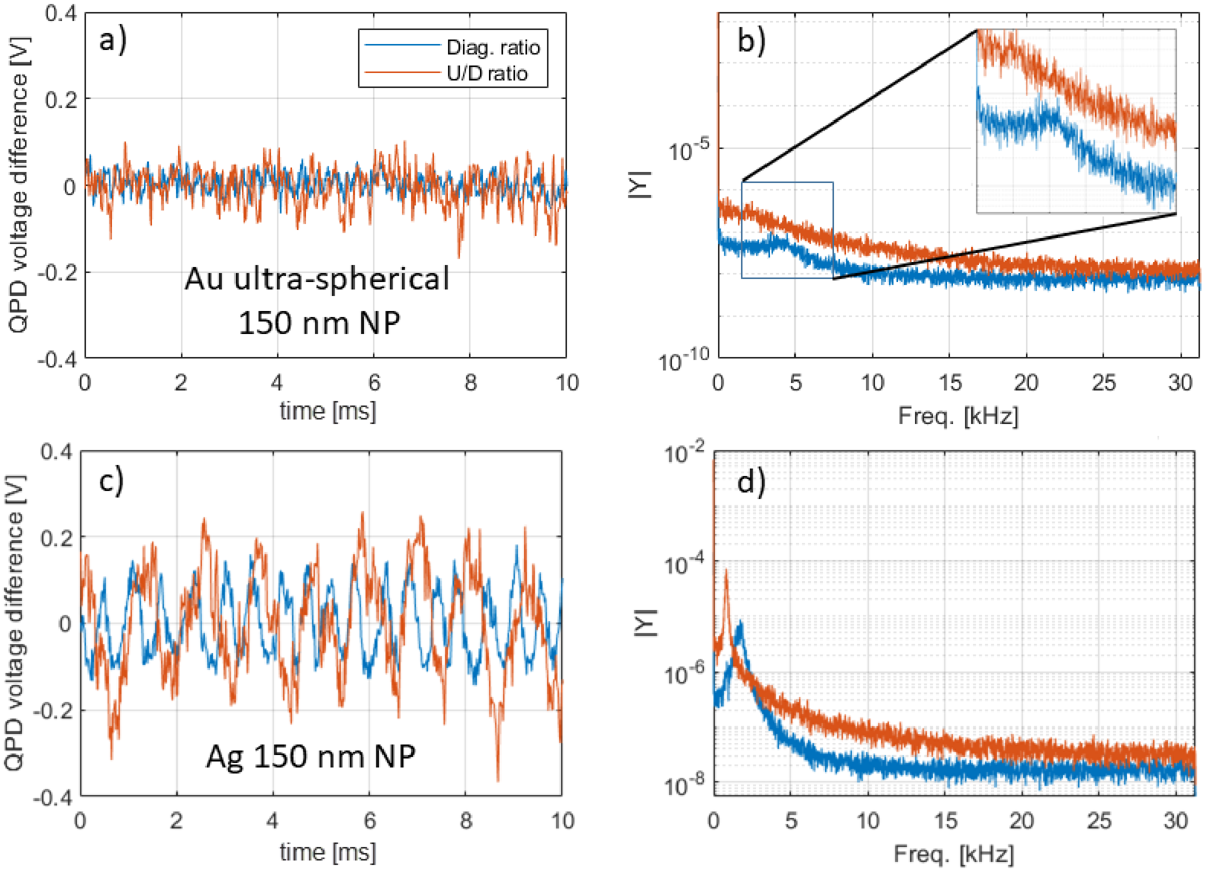

Figure S7: Comparison of experimental results from ultra-spherical Au NP and Ag NPs. (a) Time series of the diagonal and transverse (U/D) voltage ratios on the QPD for the Au ultraspherical NP. Trapping power was 4 mW. (b) PSD derived from time series shown in (a). Note the appearance of a spectral peak in the diagonal ratio at 4 kHz, which is not evident in the transverse ratio. Inset shows a zoom in on the relevant peak in the PSD. (c) Time series of the QPD voltage ratios for the Ag spherical NPs (trapping conditions are the same as for the Au NP). (d) PSD of the voltage ratios for the Ag NP shown in (c). The voltage ratio and PSD signals are significantly larger for the Ag particles due to perturbations on their surface that increase the asymmetric scattering.

S7. Raman scattering measurements of nanoparticles stuck on the coverslip surface

As described in the main text, we measured the Raman spectra of NPs optically printed onto the coverslip surface, and differentiated between particles that were optically trapped for different periods of time. The Raman measurements were performed using a Raman microscope (Horiba; HR evolution) with a laser wavelength of 473 nm. We differentiated between particles that were optically trapped for a short period of time before being stuck on the surface (less than 3 minutes), and particles that were trapped for long periods of time (longer than 3 minutes, often exceeding 7 minutes). All the particles were trapped using the same incident optical power.

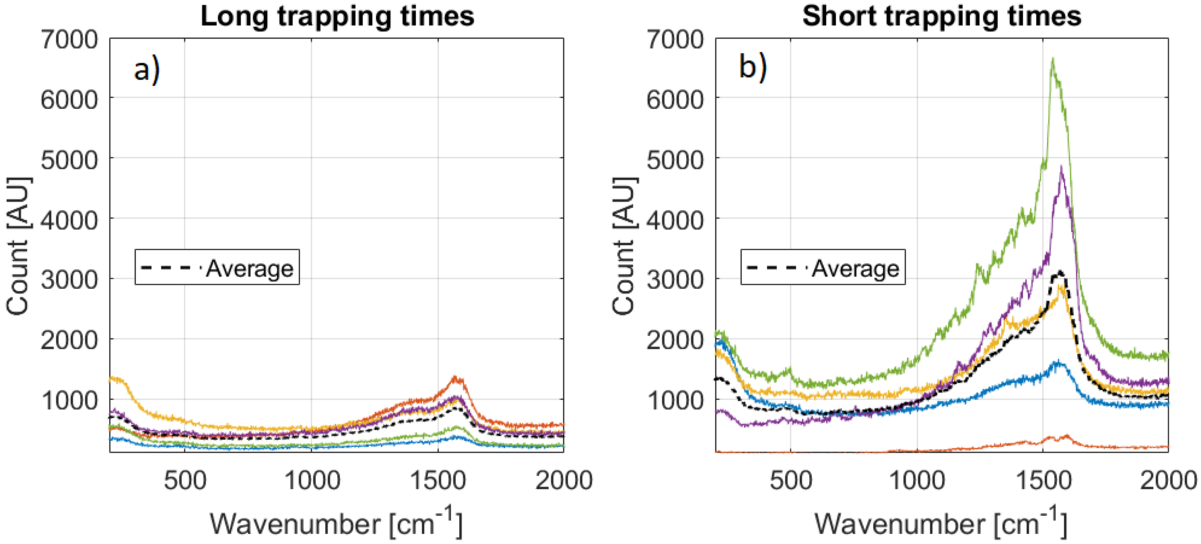

Figure S8: Raman (microscopy) spectra of single Ag nanoparticles trapped for (a) long periods of time (>3 min); (b) short periods of time (<3 min). Raman laser wavelength is 473 nm. The black dashed curves shown in both panels are the respective averages for the spectra shown. The vertical scales in the two panels are directly comparable.

Figure $S8$ shows the Raman spectra of 5 particles of each type, as well as the average spectrum (marked as a black dashed line). As can be seen, there is a significant difference in the average spectrum between the two particle classes. This is most evident at wavenumber values around 1500 cm^{-1}, where the ratio in the spectral response between the particles trapped for short times to those trapped for long times is 4. In some cases (e.g. the green curve in Figure $S8(b)$, which corresponds to a particle which was immediately printed onto the surface (see Fig. 5(c) in the main text) the ratio is even greater. The difference in the mean particle spectra implies that particles that were trapped for longer periods of time underwent more thermal induced ligand shedding than particles that were trapped for short times (especially those that were immediately trapped). As a result, the particles trapped for long times have more time to heat and shed ligands and consequently show less of a Raman signal than those particles that were trapped for short times.

The observed variance of the peak heights seen in the spectra in Figure $S8$ is due to the wide range of trapping times for both types of particles, and to differences in geometry between the NPs, which affects the density of the surface ligands, and as a result, their shedding rate in the optical trap.

S7. Processing of experimental Power Spectral Density (PSD) data

Identification of the peaks in the PSD results was done by fitting the experimentally obtained data to a modified Lorentzian function of the following form (in accordance with[S15],[S16]):

$$f = a + \frac{b}{(f - f_c)^2 + c^2} \tag{S12}$$

We compared the Lorentzian fit to a Gaussian fit. The latter would be more appropriate for spontaneous thermal motion. A general function for such a Gaussian fit is:

$$g = a + be^{-\frac{(f-f_c)^2}{\sigma^2}} \tag{S13}$$

We compared the results of the two fit functions on a representative PSD taken from the diagonal ratio of a 200 nm diameter Ag NP trapped with an optical power of 12 mW. The

PSD as well as the two functional fits are shown in Figure S9(a). Comparing the goodness of the fits, we calculate that the Gaussian fit has a $R_G^2 = 0.9395$, compared to $R_L^2 = 0.9865$. As can be seen from the fits, and the residual plots shown in Figure S9(b,c), the Lorentzian fit matches the spectral form better than the Gaussian fit, which demonstrates a rapid fall-off of the PSD as a function of frequency (in other words the peak is narrower). From this analysis, it is clear that the Lorentzians are better in the fitted figures in the main text than Gaussians.

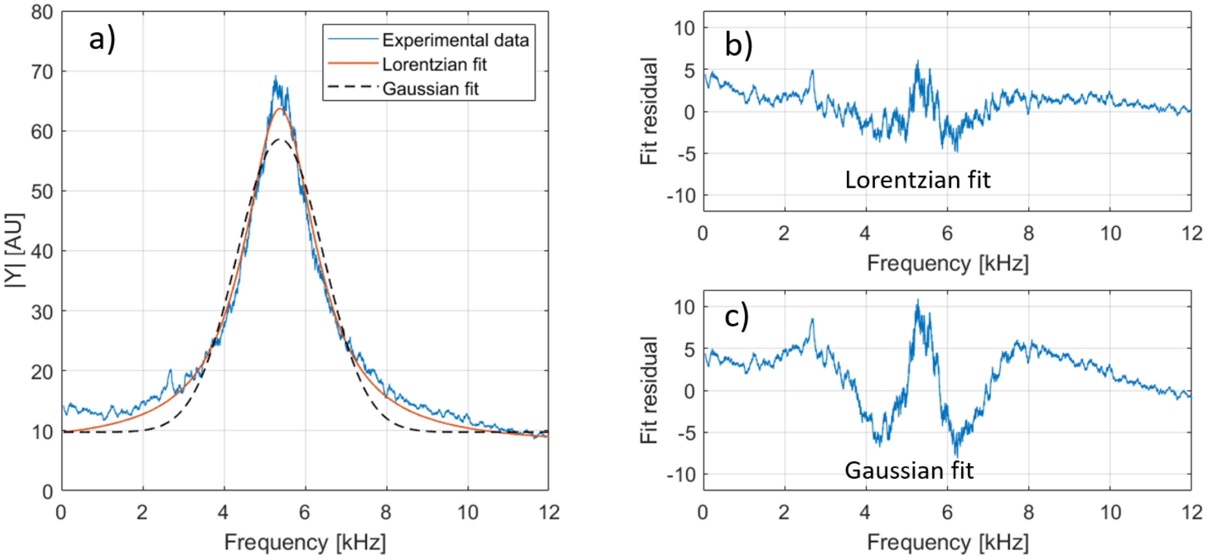

Figure S9: Comparison of different fitting functions to peaks in the PSD data. (a) Comparison of Lorentzian and Gaussian fits on experimental data using the diagonal ratio signal captured from a 200 nm Ag NP trapped with an optical power of 12 mW. Residuals of the fit for (b) Lorentian and (c) Gaussian function.s The Lorentzian function better fits the raw data.

An additional data processing method used was smoothing of the spectral data for visual purposes (not curve-fitting). In Figure S10 we demonstrate the rolling (Gaussian) filter we used and its visual effect on the data. The figures shown in the main text (e.g. Fig. 3) have been smoothed with a rolling filter of 200 samples.

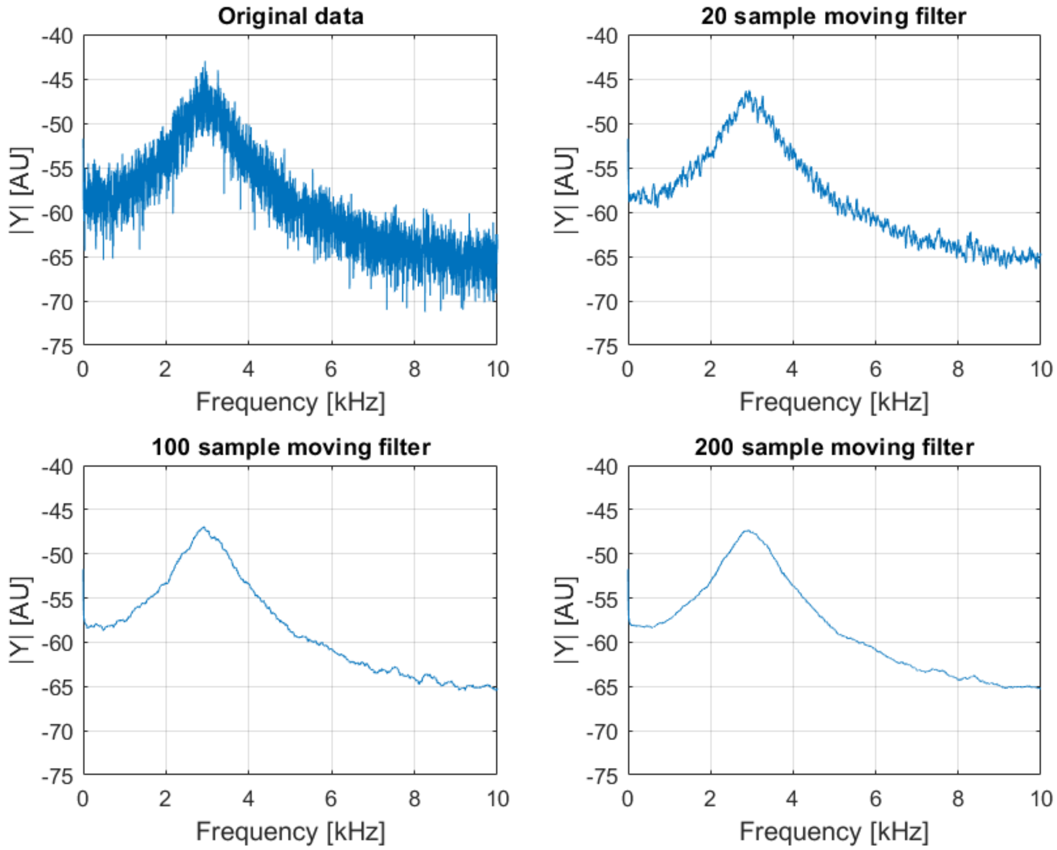

Figure S10: Application of rolling (Gaussian) filter to experimental PSD data. These graphs show the PSD of a diagonal ratio of a 150 nm Ag NP trapped in a optical trap with a power of 12 mW (data presented in Figure 3(a) in the main text. PSDs shown have different values of moving filters (a) No filtering, (b) 20 samples (c) 100 samples, (d) 200 samples. Note that curve fitting and peak localization were done on unfiltered data.

References

(S1) Lehmuskero, A.; Ogier, R.; Gschneidtner, T.; Johansson, P.; Kall, M. *Nano letters* **2013**, *13*, 3129–3134.

(S2) Deng, T.-S.; Parker, J.; Hirai, Y.; Shepherd, N.; Yabu, H.; Scherer, N. F. *physica status solidi (b)* **2020**, *257*, 2000169.

(S3) Yifat, Y.; Coursault, D.; Peterson, C. W.; Parker, J.; Bao, Y.; Gray, S. K.; Rice, S. A.; Scherer, N. F. *Light: Science & Applications* **2018**, *7*, 1–7.

(S4) Waterman, P. *Proceedings of the IEEE* **1965**, *53*, 805–812.

(S5) Doicu, A.; Wriedt, T.; Eremin, Y. A. *Light scattering by systems of particles: null-field method with discrete sources: theory and programs*; Springer, 2006; Vol. 124.

(S6) Taylor, J.; Love, G. *JOSA A* **2009**, *26*, 278–282.

(S7) Barton, J.; Alexander, D.; Schaub, S. *Journal of Applied Physics* **1989**, *66*, 4594–4602.

(S8) Kim, S.; Karrila, S. J. *Microhydrodynamics: principles and selected applications*; Courier Corporation, 2013.

(S9) Kuipers, J. B. *Quaternions and rotation sequences: a primer with applications to orbits, aerospace, and virtual reality*; Princeton university press, 1999.

(S10) Xu, Y.-l. *Physical Review E* **2003**, *67*, 046620.

(S11) Simpson, S. H.; Hanna, S. *JOSA A* **2007**, *24*, 430–443.

(S12) Li, M.; Yan, S.; Yao, B.; Liang, Y.; Han, G.; Zhang, P. *JOSA A* **2016**, *33*, 1341–1347.

(S13) Johnson, P. B.; Christy, R.-W. *Physical review B* **1972**, *6*, 4370.

(S14) `https://www.lumerical.com/products/`.

(S15) Berg-Sørensen, K.; Flyvbjerg, H. *Review of Scientific Instruments* **2004**, *75*, 594–612.

(S16) Perkins, T. T. *Laser & Photonics Reviews* **2009**, *3*, 203–220.